https://doi.org/10.26599/FRICT.2026.9441262
Research Article

Novel surface engineering design enabled surface multi-functionalisation of metastable Ti-15-3 β-titanium alloy

Tong Pan[a], Xuan Huang[a], Behnam Dashtbozorg[a], Siyu Sun[a], Yepeng Yang[a], Ke Ren[c*], Artemis Stamboulis[a], Xiaoying Li[a], Kan Ma[b,a*], Hanshan Dong[a]

[a] School of Metallurgy and Materials, University of Birmingham, Edgbaston, Birmingham, B15 2TT, UK.

[b] Department of Mechanical Engineering, City University of Hong Kong, Hong Kong, China.

[c] School of Chemical Engineering, University of Birmingham, Edgbaston, Birmingham, B15 2TT, UK.

[*] Corresponding authors:

Ke Ren, E-mail: k.ren@bham.ac.uk;

Kan Ma, E-mail: kan.ma@cityu.edu.hk.

Received: January 3, 2026; Revised: March 10, 2026; Accepted: May 7, 2026

Abstract

The growing demand for high-performance and long-service components for challenging and resource-intensive applications has driven the development of high-strength metastable β-titanium alloys with multi-functional surfaces. In this study, a novel surface engineering strategy, termed integrated bulk heat treatment with surface functionalisation (IBTSF), is introduced. This approach combines bulk ageing treatment with catalytic ceramic conversion treatment (C3T) incorporating Ag or Au, thereby simultaneously imparting surface multi-functionalities (high hardness, desirable tribological properties and high antibacterial efficacy) while also enhancing the bulk mechanical properties. To this end, the metastable β-alloy Ti-15V-3Al-3Cr-3Sn (Ti-15-3) was selected as a representative alloy, and C3T was catalysed using either Au or Ag. Under a load of 20 N, the Au-catalysed C3T achieved near-zero wear and a low, stable coefficient of friction of ~0.3, owing to the formation of a lubricating tribo-film. In contrast, the Ag-catalysed C3T maintained stable tribological performance up to a load of 10 N while delivering high antibacterial efficacies of 99.878% and 99.999% against *E. coli* and *S. aureus* within 3 h and 6 h of contact, respectively, through passive Ag-ion release. Both treatments also enhanced the bulk tensile strength by approximately 50%, increasing from 872 ± 39 MPa to 1280 ± 40 MPa. This combination of exceptional wear resistance, potent antibacterial activity, and improved mechanical strength offers a promising and efficient pathway to the surface multi-functionalising metastable alloys for long-service, high-reliability applications.

Keywords: Ti-15-3; Metastable β-titanium alloy; Multi-functionalisation; Wear resistance; Antibacterial; Catalytic ceramic conversion treatment (C3T).

1. Introduction

The wear behaviour of high-performance materials often involves interaction with complex biological environments, which can accelerate material degradation and, in some cases, lead to biological hazards or health risks. For example, marine equipment is subjected to simultaneous wear and micro-biologically influenced corrosion (MIC) [1-4]; debris released from biomedical implants can trigger inflammatory responses once it enters the bloodstream [5-9]. It is well documented that wear can not only introduce immunogenic Ti nanoparticles associated with inflammatory response, but can also enlarge micro-gaps at the implant-abutment interface in two-piece dental implant systems, enabling bacterial ingress and subsequent mechanical and biological complications [10, 11]. These scenarios underscore the growing demand for multi-functional materials surfaces that offer both mechanical durability and antibacterial functionality, thereby supporting safer, longer-lasting, and more resource-efficient technologies.

Titanium alloys, known for their high strength-to-weight ratio, outstanding corrosion resistance, and good biocompatibility [12-15], are promising candidates for marine and biomedical applications. However, Ti and its alloys exhibit inherently poor tribological performance [16]. Accordingly, surface engineering strategies have been employed to overcome this limitation by increasing surface hardness and suppressing adhesive wear, primarily by isolating reactive Ti atoms (unfilled [Ar] $4s^2 3d^2$ configuration) from direct contact during sliding [17-22]. For instance, a laser clad CrMoNbW–10 wt% Cu coating achieves a sixfold increase in hardness and approximately 69-fold improvement in wear resistance under a 1 N load compared with Ti-6Al-4V, while the Cu addition provides an 88% reduction of viable bacteria via Cu^+ ion release [23]. However, such hard coatings often suffer from high interfacial stress concentrations during rapid cooling in laser cladding and mechanical loading during service due to differences in Young's modulus and thermal expansion coefficients between the coating and the substrate. These stresses can lead to poor adhesion and eventual delamination. To mitigate this problem, a ternary surface modification combining laser surface texturing (LST), plasma

nitriding, and a functional lubricant (Ag_2O-MSNs@OTES) has been explored [13, 24, 25]. However, the poor thermal stability and weak interfacial adhesion of the lubricant layer, along with the high cost and multi-step processing complexity, continue to obstruct its practical utilisation. In our previous work, an advanced ceramic conversion treatment (C2T) was developed to effectively improve the wear resistance of CP-Ti and α-β Ti alloys [26, 27].

To meet the requirements for multi-functional properties and good formability, metastable β-titanium alloys are an excellent choice as substrate materials due to their high strength, good ductility, superior cold formability, excellent hardening capability, and adjustable mechanical properties [28-31]. However, like α and α-β Ti alloys, β-titanium alloys also suffer from poor tribological performance. The C2T treatment is not suitable for these alloys as it employs temperatures above 600 ℃ for at least 50 hours to achieve sufficiently thick oxide layer. These conditions lead to excessive β grain growth and undesirable α precipitation in metastable β-titanium alloys [32], ultimately degrading their bulk mechanical performance due to over-ageing. Our recent breakthrough in rapid catalytic C2T (or C3T) using a catalytic element has enabled significant reductions in the treatment temperature and time [26, 27, 33, 34].

Therefore, the technical challenge of applying C2T to metastable β-titanium alloys can be addressed through a specially developed integration of bulk heat treatment (BT) with catalytic ceramic conversion treatment (C3T) for β-titanium alloys. This combined approach simultaneously generates wear-resistant surfaces and strengthens the bulk mechanical properties during ageing, while avoiding the additional energy consumption associated with the separate treatments. After high-temperature solution treatment, the oxide layer was removed and a catalytic gold (Au) layer was deposited. Subsequent C3T generated a new oxide layer with desirable microstructure, improved wear properties and enhanced interfacial bonding for the low-cost beta (β) alloy originally developed for cost-effective suspension springs in racing and high-end cars [33, 34].

To satisfy the increasing demand for high bulk strength, multi-functional surface properties (tribological, corrosion and antibacterial) and excellent formability for cost-effective manufacturing, a novel surface engineering strategy has been developed. This study integrates bulk ageing of the metastable β-titanium alloy Ti-15V-3Al-3Cr-3Sn (Ti-15-3) with silver (Ag)-facilitated C3T surface functionalisation (IBTSF). Ti-15-3 is specifically engineered to provide high-strength via ageing, excellent formability, and high corrosion resistance for demanding applications in aerospace, automotive systems, and medical industries [35, 36]. To this end, Ti-15-3 was subjected to various IBTSF strategies using Ag as well as Au for comparison. Surface performance was evaluated using wear tests and antibacterial tests, while bulk mechanical properties were assessed using profilometry-based indentation plastometry (PIP). The findings demonstrate that this novel IBTSF surface engineering design can generate multi-functional surfaces exhibiting both desirable tribological properties and high antibacterial efficacy on high-strength Ti-15-3 alloys. This work extends the applicability of ceramic conversion treatments and provides a new pathway for surface multi-functionalisation of titanium alloys.

2. Experimental

2.1 Material and sample preparation

The β-titanium alloy Ti-15V-3Al-3Cr-3Sn (Ti-15-3, National Institute of Standards and Technology, United States) with the following composition (wt.%): 15% V, 3% Al, 3% Cr, 3% Sn, and balance Ti was used for this study. The 4 cm diameter rod was sectioned into 5 mm-thick coupons, and their surfaces were ground to 1200-grit. The samples were then ultrasonically cleaned in acetone and then dried with hot air prior to further analysis and treatment.

2.2 Design of the integration of bulk treatment with surface multi-functionalisation (IBTSF)

A novel integrated bulk strengthening and surface multi-functionalisation technique, IBTSF, was specifically designed for metastable β-titanium alloys. To prevent excessive α precipitation during the subsequent C3T, the as-received Ti-15-3 was first solution treated (ST), as shown in **Figure 1**. The material was heated at a rate of 10 ℃/min to 850 ℃, slightly above the β-transus of Ti-15-3 (~800-820℃) [37, 38], and held for 1 hour, followed by rapid water quenching to retain a predominantly β-phase microstructure at room temperature. This pre-treatment homogenises alloying elements in the β matrix and relieves residual stresses, thereby establishing a stable β microstructure prior to catalytic oxidation [39].

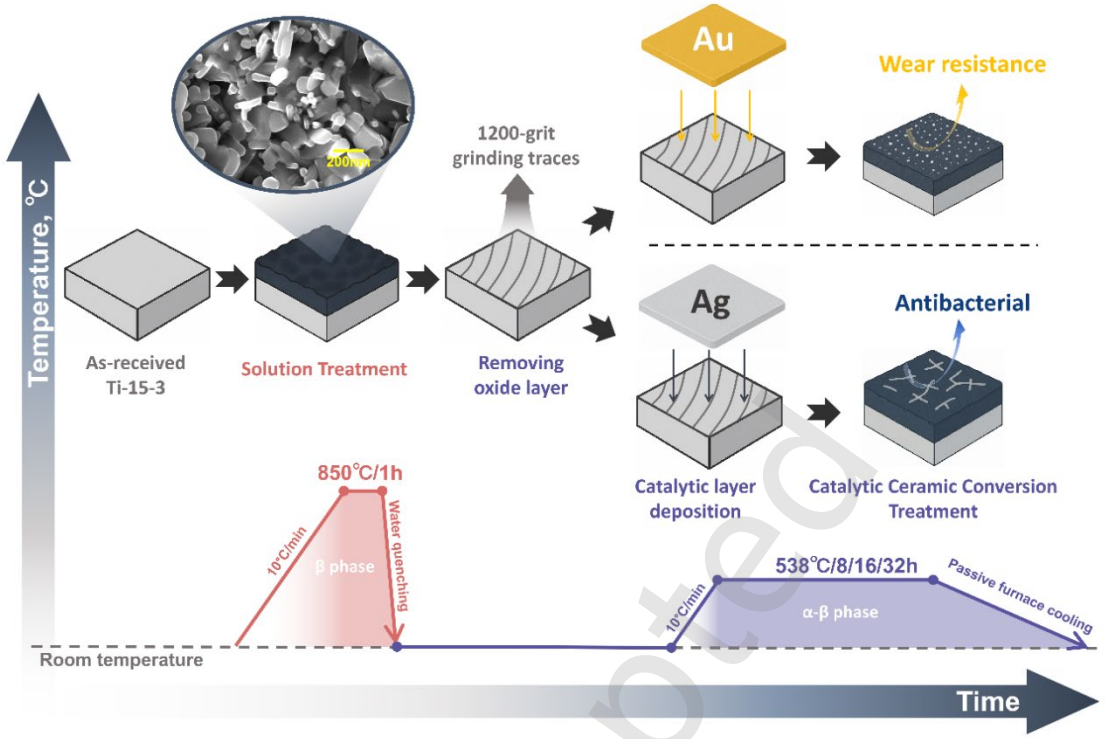

Figure 1. Schematic diagram of the novel IBTSF technique.

The surface oxide layer formed during the ST, consisting of columnar crystals (**Figure 1**) with poor interfacial quality [34], was removed by 1200-grit grinding. A 20 nm layer of Ag (or Au for comparison) was then deposited onto the surface of the ST samples by sputter coating using a Quorum Q150T ES sputter coater (Quorum Technologies, UK). Finally, the integrated bulk ageing and surface functionalisation treatment via Catalytic Ceramic Conversion Treatment (C3T) was performed at 538 ℃, the optimal ageing temperature for Ti-15-3 [33, 40], in an Elite Thermal Systems Limited electric furnace. The material was heated at a rate of 10 ℃/min and held for 8, 16 and 32 hours before furnace cooling. This process generated a high-quality multi-functional ceramic layer doped with Ag (C3TAg) or Au (C3TAu) through C3T while simultaneously strengthening the bulk material through optimal ageing.

For comparison, selected ST samples were also directly aged (ST-A) at 538 ℃ for 8, 16 and 32 h in air, or subjected to ceramic conversion treatment (C2T) using the same conditions but with no pre-deposited catalytic film. The specimen codes and corresponding processing parameters are summarised in **Table 1**.

Table 1. Specimen codes with corresponding processing parameters.

Specimen code	Catalytic layer	Ageing time (h) at 538 °C		
		8	16	32
ST	-	ST-A8	ST-A16	ST-A32
C2T	-	C2T8	C2T16	C2T32
C3TAu	Au (20nm)	C3TAu8	C3TAu16	C3TAu32
C3TAg	Ag (20nm)	C3TAg8	C3TAg16	C3TAg32

2.3 Microstructure characterisation

Scanning electron microscopy (SEM) and energy-dispersive x-ray spectroscopy (EDS) were carried out using a Thermo Fisher Scientific Apreo 2S HiVac (Thermo Fisher Scientific, USA). Phase constituents of all the samples were analysed by X-ray diffraction (XRD) using a Proto X-ray diffractometer (Proto Manufacturing, Canada) with Cu Kα radiation (λ = 1.5406 Å) over a 2θ range of 20-80°. Phase identification was performed using the HighScore software package (Panalytical B.V., Netherlands) based on the ICDD PDF-2 database. Electron backscatter diffraction (EBSD) was performed on a JEOL JSM-7000F (JEOL, Japan) equipped with an EBSD detector (Oxford Instruments, UK) to map the phase distribution. The final polishing for EBSD samples was performed using a 1:1 mixture of hydrogen peroxide and colloidal silica (OPS) for 15 minutes.

Cross-sectional TEM specimens were prepared using a CIQTEK DB550 focused ion beam scanning electron microscope (FIB-SEM) (CIQTEK, China). Transmission electron microscopy (TEM) analysis was conducted using a Talos F200X G2 TEM (Thermo Fisher Scientific, USA) equipped with an energy-dispersive X-ray spectroscopy (EDS) system (Oxford Instruments, UK) to characterise the microstructure and elemental distribution.

2.4 Mechanical property evaluation

Surface roughness (Ra, arithmetic average roughness) was measured using an Ambio Technology XP-200 machine along a measurement distance of 5 mm

and a scan speed of 0.01 mm/s. Ra measurements were repeated 3 times, and the average value has been reported. Surface hardness was measured using a Vickers hardness indenter under loads of 25, 50, 100, 200, and 300 gf. The interval between every two indentations was at least 3 times the diagonal length of the indentations, and the average value of 10 repeated measurements was reported for each sample.

Profilometry-Based Indentation Plastometry (PIP) tests were performed to assess the bulk mechanical properties of all the Ti-15-3 samples. Each test was conducted 3 times using a PLX-benchtop system (Plastometrex, UK), which combines spherical indentation with iterative finite element method (FEM) modelling to determine the bulk stress–strain relationship [41, 42]. A spherical indenter with a radius (R) of 0.5 mm was employed, with an effective displacement (δ) of approximately 100~200μm (δ/R≈10~20%). Indentation profiles were recorded along two perpendicular directions (depth and radial position) through the central axis of the indent using the integrated profilometry system and subsequently compared with FEM-simulated profiles to extract material-specific mechanical parameters. The nominal stress-strain curves were calculated from the measured indenter displacement and applied load, while the true stress-strain relationships were established using the Voce equation [43], which accounts for real-time changes in the cross-sectional area and length of Ti-15-3, thereby providing a more accurate representation of mechanical behaviour:

$$\sigma = \sigma_S - (\sigma_S - \sigma_Y) exp(-\varepsilon/\varepsilon_0) \quad (1)$$

where σ is applied stress; σ_S is a saturation level; σ_Y is the yield stress; ε_0 is a characteristic strain describing the exponential approach of the stress towards the saturation level. All the measurements were performed 3 times at different regions of each sample to ensure statistical reliability.

2.5 Tribological behaviour assessment

To investigate the tribological performances of the various surface treated samples, reciprocating sliding wear tests were conducted on 32h-treated samples including ST-A32, C2T32, C3TAu32, C3TAg32 against an 8 mm tungsten carbide ball (WC). The test for each sample was repeated 3 times with

a sliding distance of 5 mm and sliding speed of 5 mm/s for 1000 cycles. These tests were performed under loads of 10 N and 20 N using a TE-79 multi-axis tribometer (Phoenix Tribology, UK) under air and room temperature (22±3 ℃) conditions. The wear factor (K, $m^3/N{\cdot}m$) was calculated using:

$$K = \frac{V}{F \times s} = \frac{A \times 5 \times 10^{-3}}{F \times s} \quad (2)$$

where V is the wear volume (m^3), F is the applied load (N), s is the sliding distance (m), A is the cross-sectional area of the wear scar (m^2) calculated based on the depth profiles measured by a profilometer [33]. Surface topography of the wear track was characterised using a white light interferometer (Profilm3D, KLA Corporation, California, USA) equipped with a Nikon CF Plan objective lens (Nikon Corporation, Japan).

2.6 Antibacterial performance tests

The Miles and Misra method was used to assess the antibacterial properties of the Ti samples. *Staphylococcus aureus* (ATCC 25923) and *Escherichia coli* (ATCC 25992) were used as model Gram-positive and Gram-negative organisms, respectively, to evaluate the antibacterial performance of the multi-functional surfaces developed in this study. Specimens were cut into 1 cm × 1 cm pieces, immersed in 70% industrial methylated spirit for 30 minutes, and then air-dried under sterile conditions. Subsequently, the sterile specimens were aseptically placed into 96-well culture plates. Bacterial strains were grown in Luria-Bertani (LB) broth at 37 ℃ to prepare bacterial suspensions. The bacterial concentration was determined by measuring optical density at 600 nm (OD_{600}) using a Jenway 5300 spectrophotometer. Initial suspensions were adjusted to achieve 1×10^6 CFU/ml, and 100 μl aliquots were used to immerse specimen within the well culture plates. Samples were incubated in the dark for 3 and 6 h.

Following incubation, each specimen was rinsed with 200 μl of phosphate-buffered saline (PBS) to dislodge the remaining bacteria into the solution. This suspension was serially diluted down to concentrations of 10^{-7}, relative to the initial incubated suspension. From each appropriate dilution, three 20 μl drops were placed onto separate quadrants of nutrient agar plates. After drying, plates

were incubated at 37 ℃ for 24 h to allow for viable bacteria to form visible colony forming units (CFU) for plate counting. High bacterial concentrations that resulted in confluent growth across the drop area were not used for quantitative analysis. Only quadrants containing 1-50 CFUs were used to evaluate antibacterial activity. The CFU concentration was calculated as follows:

$$\mathrm{CFU/\ mL}=\mathrm{A_c}\times\mathrm{D_f}\times 50 \tag{3}$$

where $\mathrm{A_c}$ is the average colony count for a given dilution, and $\mathrm{D_f}$ is the dilution factor of the drop, defined as the volume of the original solution divided by the total volume of the diluted suspension, and 50 is the correction factor for the 20 μl aliquots.

The antibacterial rate, R, of each sample type was calculated according to the following formula:

$$\mathrm{R}=\frac{\mathrm{N_{control}}-\mathrm{N_{sample}}}{\mathrm{N_{control}}}\times 100\% \tag{4}$$

where, $N_{control}$ and N_{sample} are the bacterial concentration of the untreated and treated samples, respectively.

3. Results

3.1 Surface roughness and morphology

To investigate the effects of the multiple surface treatments developed from this research, the study first examines the surface roughness profiles and morphological features. **Figure 2a** presents the surface roughness trends (Ra, arithmetic average roughness), measured perpendicular to the original 1200 grinding traces of the ST samples. In addition, the corresponding SEM images of all treated surfaces and the EDS mapping for the 8h treated C2T8 (**Figure 2b**), C3TAu8 (**Figure 2c**) and C3TAg8 (**Figure 2d**) samples are also illustrated. As shown in **Figure 2a**, the Ra of C2T8 is marginally lower than that of the ST baseline (dashed line, Ra ≈ 0.32μm) mainly due to the formation of a thin titanium oxide film, although the grinding marks remain visible (**Figure 2b**).

On the contrary, the Ra value of the C3TAg samples exceeds that of the ST baseline. This is attributed to the presence of large, randomly distributed Ag-V surface features that overlay the original grinding marks (**Figure 2d**). These features dominate the surface roughness and contributed substantially to the elevated Ra values of C3TAg. Additionally, the surface is expected to be rougher due to the continued growth of Ag-V compounds (**Figure 2a** and **Figure S3**).

The Ra of the C3TAu samples is much lower than that of C3TAg and is also comfortably below the ST baseline. However, Au has an intrinsic tendency agglomerate [44] and its catalytic effect on oxidation [33] leads to localised oxide growth around large Au particles. This is evident from the white particles observed in SEM images, which correspond to Au-rich zones in EDS maps (**Figure 2c**). This results in rapid rounding of the grinding marks within the first 8h and a corresponding decrease in Ra relative to ST. However, as the oxide continues to grow unevenly around these Au particles (**Figure S2**), Ra increases again from 16 to 32h (**Figure 2a**). In contrast, EDS mapping (**Figure 2**) reveals that, unlike C3TAg32 and C3TAu32, both of which exhibit distinct surface features, the surface of the C2T32 sample was rich in O, Ti and V, indicating the formation of titanium and vanadium oxides. Without a catalytic film, the oxide growth on C2T samples is slow, leaving the surface primarily in

the stage of progressive smoothing of the initial 1200-grit grooves, and therefore resulting in the continuous reduction in Ra.

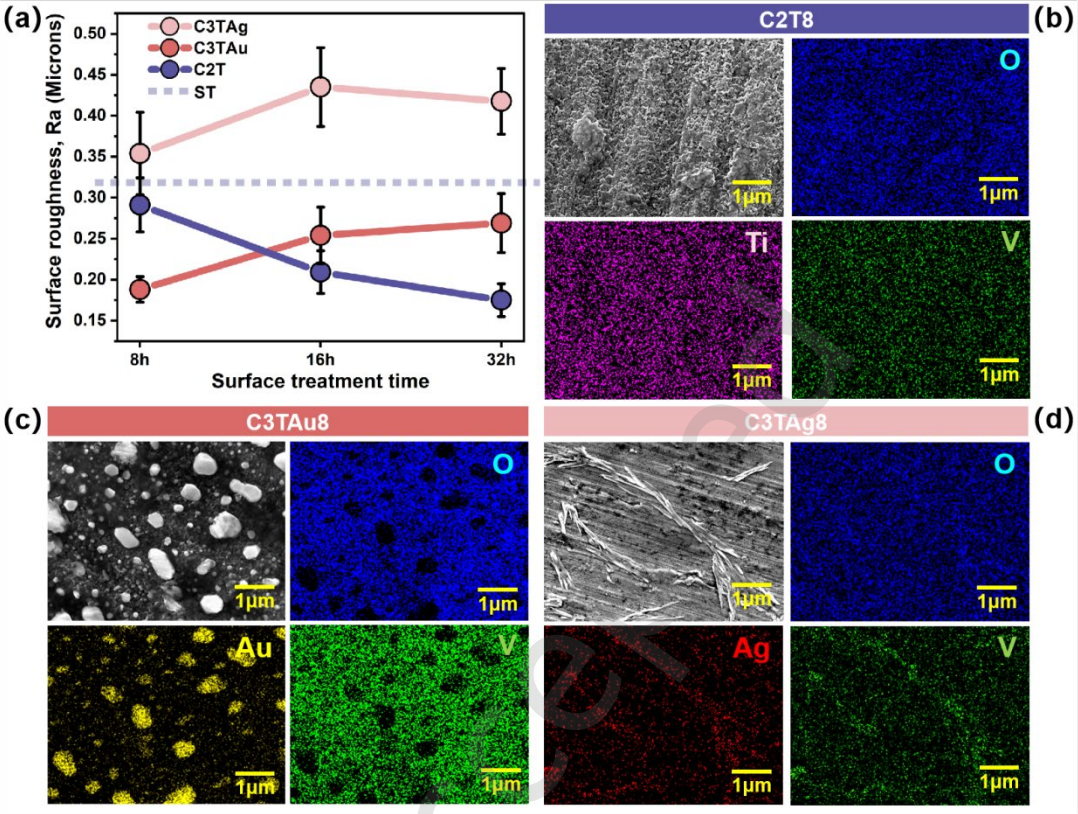

Figure 2. (a) Surface roughness (Ra) as a function of treatment time, and surface SEM/EDS elements mapping for 8h treated (b) C2T8, (c) C3TAu8 and (d) C3TAg8 samples.

From **Figure 2**, it can be seen that although the oxidation duration from 8h to 16h is only half that of the 16-32h interval, the changes in Ra are more pronounced in the earlier periods (**Figure 2**). This suggests that the oxidation may follow the parabolic law over time, likely due to the barrier effect created by the dense oxide layer formed at the early stage, which hinders further oxide growth.

3.2 Surface layer structures

To provide multi-dimensional characterisation of the treated surfaces, cross-sectional analyses were carried on all samples. For each oxidation duration, the oxide layer thickness followed the trend: C3TAg > C3TAu > C2T (**Figure 3** & **Figure S4**). For example, the oxide layer thickness in C3TAg32 reached ~3 μm, compared to ~1.6 μm in C3TAu32 and ~0.8 μm in C2T32 (**Figure S4**).

These findings confirm the catalytic enhancement of oxide growth by C3T and demonstrate that Ag catalysis is more effective than Au.

Under the same catalytic conditions, the oxide thickness increased with oxidation duration; however, the growth rate gradually decreased over time. For instance, when increasing the oxidation time from 8 to 16 h, the oxide thickness of C3TAg rose from ~1.3 μm to ~2.6 μm (~100% increase, **Figure 3**), while the subsequent increase to ~3 μm at 32 h represented a growth of only ~13%. This trend mirrors with the surface roughness evolution of C3T discussed in **Section 3.1**, further indicating a progressive reduction in oxidation kinetics over time.

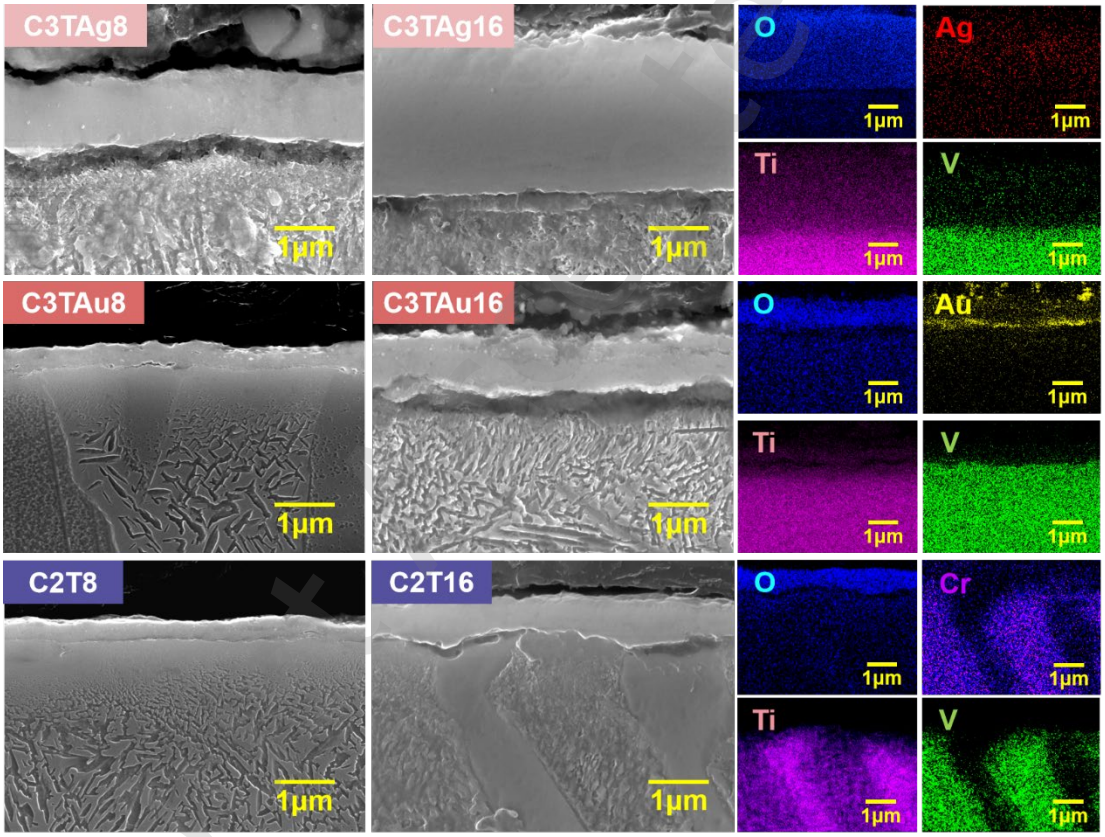

Figure 3. Surface layer structure of C2T & C3T samples after 8, 16 h treatments and EDS mapping of the 16 h treated samples.

EDS mapping revealed distinct elemental distributions in the oxide layers after the fast oxidation reaction stage between 8-16 h (**Figure 3**). Ag was found to be homogeneously distributed throughout the oxide layer of the C3TAg16 sample. In contrast, for the C3TAu16 sample, Au appeared not only as agglomerated surface particles (**Figure 2**) but also as dispersed nano-scale clusters within the oxide layer and at the oxide/substrate interface, as shown in

the C3TAu16 EDS map in **Figure 3**. These elemental distributions are expected to influence the mechanical integrity of the oxide layer, which will be discussed in **Section 3.3**. For the C2T16 sample, EDS mapping revealed lath-like Ti-enriched regions beneath the oxide layer but within the oxygen diffusion zone (ODZ). EBSD phase maps (**Figure 4a**) confirm these regions to be α-Ti (hcp), which has precipitated from the strong alpha stabilisation effect of oxygen. These α-Ti precipitates are found along grain boundaries and within grains in both vertical and horizontal orientations. This α-phase precipitation in the ODZ is expected to provide mechanical support to the surface oxide layer during hardness testing, as discussed in **Section 3.3**.

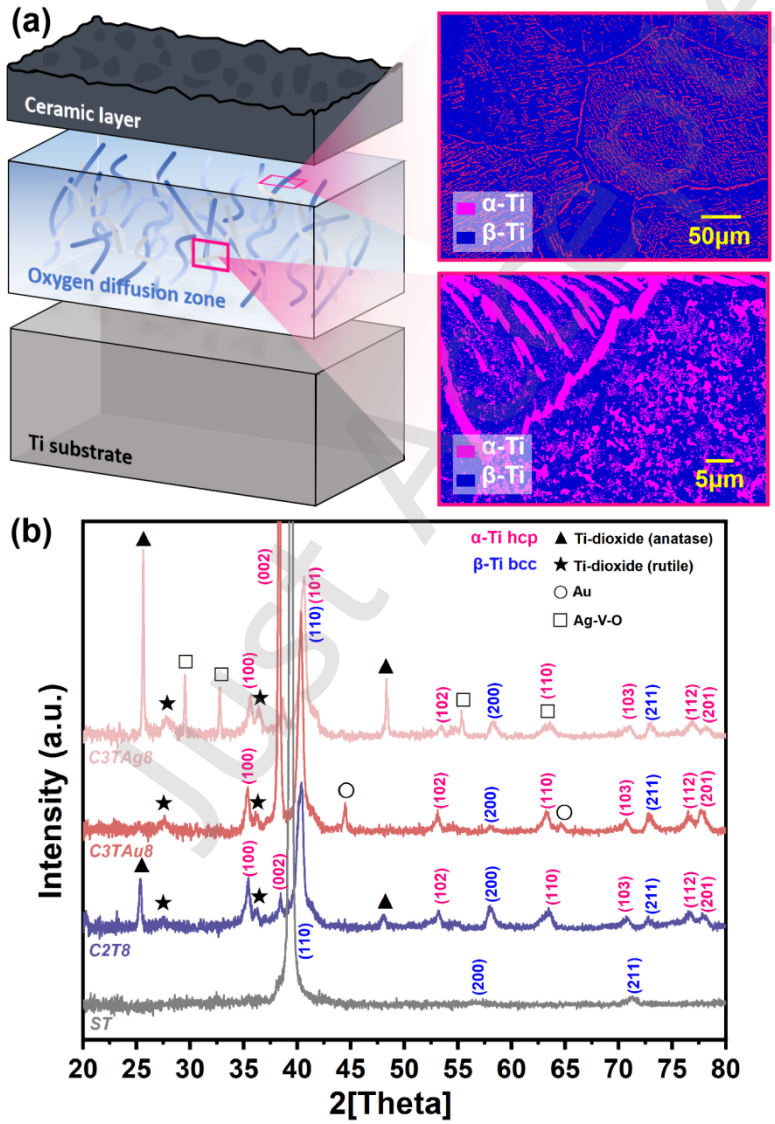

Figure 4. (a) Phase distribution of C2T16 ODZ; (b) XRD patterns of ST and 8 h treated samples.

The mechanism for Au catalysis can be attributed to its high electronegativity, which facilitates electron withdrawal from Ti atoms, thus promoting their oxidation as Ti ions capable of forming TiO_2 [33]. In contrast, the superior oxidation-promoting effect of Ag is likely due to its intrinsic oxidation tendency and its specific promotion of vanadium oxidation. This is supported by the presence of Ag-V oxide peaks in the XRD patterns of C3TAg8 at 2θ = 29.6°, 32.8°, and 55.5° ($AgVO_3$, reference code: 00-029-1154, **Figure 4b**), as well as by the surface features of Ag-V-O observed in **Figure 2**. In addition, it is surprising to find that anatase-TiO_2 peaks (at 25.7° and 48.8°) are detected in C2T8 and C3TAg8, but not in C3TAu8 samples. Such differences imply distinct mechanisms underlying wear and antibacterial properties, which will be discussed in **Section 4**.

3.3 Surface and bulk mechanical properties

To validate the effects of these surface treatments on the material properties, **Figure 5** presents a comprehensive comparison of the surface hardness of different C2T and C3T samples by Vickers indentation tests, alongside an evaluation of the influence of C3T on the bulk mechanical properties using Profilometry-based Indentation Plastometry (PIP).

In terms of surface hardness (**Figure 5a**), C3TAg samples exhibited the highest hardness values under low loads (≤100 gf), followed by C2T, while C3TAu samples showed the lowest values for the same oxidation durations. This reduction in hardness for C3TAu is attributed to the intrinsic softness of Au nano-particles embedded within the oxide layer. In addition, the interfacial Au (EDS mapping, **Figure 3**), which is inherently soft, can also act as a buffer, mitigating the stress concentration imposed by Vickers indentation. In contrast, due to its high oxidation tendency, most of the Ag accumulated at the surface to form surface Ag-V oxides (**Figure 2**), which contributed to the high surface hardness of C3TAg samples, although the clustered Ag-V oxide also introduced substantial variation in the measurements. Moreover, **Figure 5a** indicates that extending the oxidation duration has a limited effect in improving the surface hardness of the C3TAu samples, which may be attributed to the distinct single-phase oxide structure revealed by XRD. For C2T samples, surface hardness was found to increase with treatment time. This improvement in the measured

surface hardness can be attributed to both oxide layer thickening and the formation of a reinforcing oxygen diffusion zone (ODZ) (**Figure 4a**).

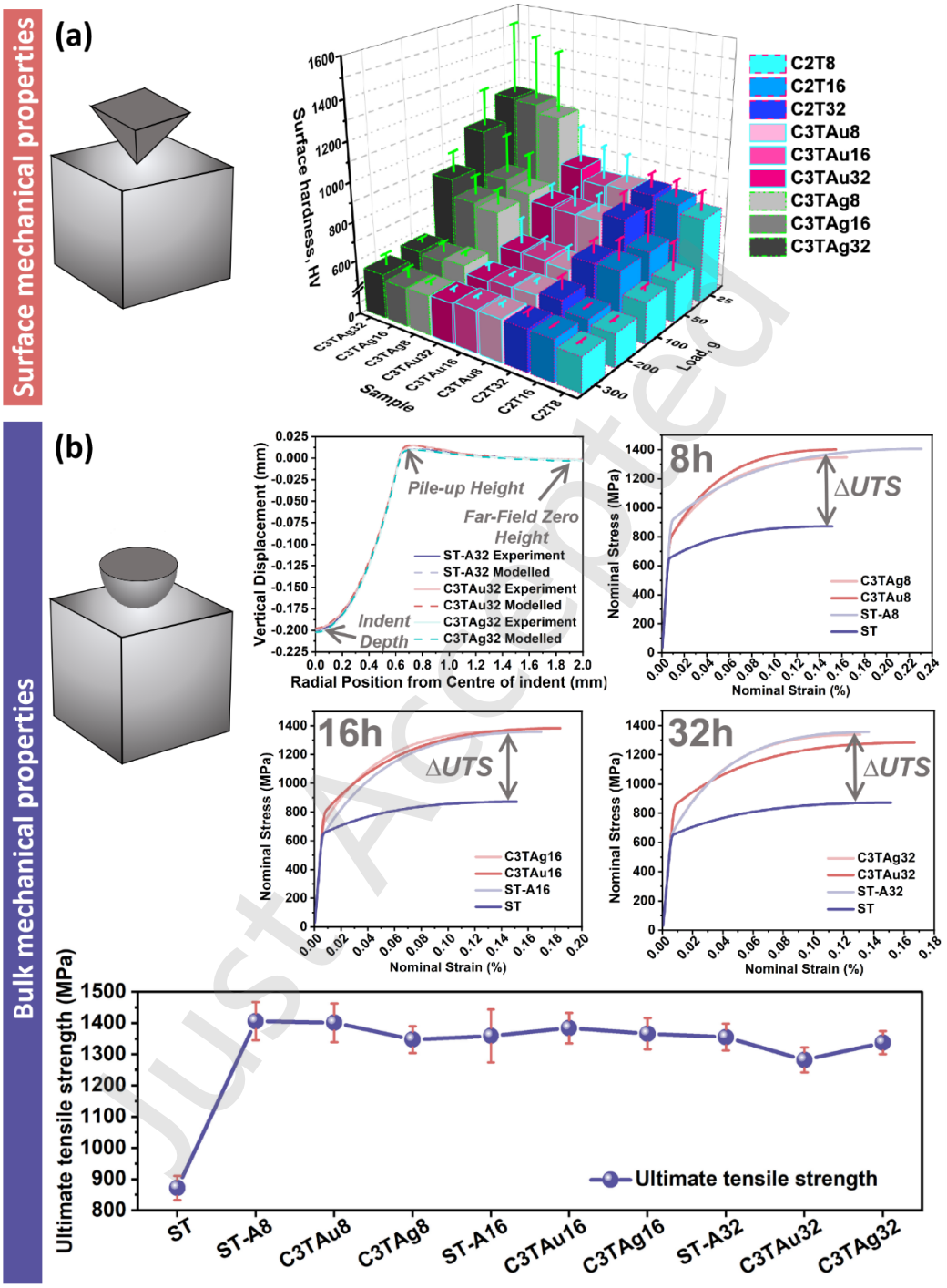

Figure 5. (a) Surface hardness & load-bearing capacity; (b) Bulk mechanical properties measured by profilometry-based indentation plastometry (PIP) testing.

To verify whether C2T and C3T affect the improvement of bulk mechanical properties during the integrated bulk ageing and surface ceramic conversion

treatment, an advanced PIP technique was employed for rapid evaluation of the bulk mechanical properties of the treated samples. The experimental indentation profiles showed excellent agreement with the modelled profiles (**Figure 5b**), confirming the accuracy and reliability of the PIP approach for evaluating bulk mechanical performance in surface treated Ti-15-3. The stress-strain curves generated using the PIP method revealed that C3TAu and C3TAg samples exhibited nearly identical ultimate tensile strength (UTS) to that of the ST-A sample, and were significantly higher than the ST sample. This indicates that the C3T component of the designed IBTSF treatment can not only impart potential surface multi-functionality but also improve bulk mechanical strength similar to traditional ST-A, through the transformation of a portion of β-Ti (bcc) into fine α-Ti (hcp) precipitates (**Figure 4b**). As shown in **Figure 5b**, the UTS increased from 872 ± 39 MPa for the ST samples to over 1282 ± 40 MPa for the C3T samples, indicating an increase of approximately 400 MPa (ΔUTS ≈ 50%). These findings demonstrate that C3T has been successfully integrated with traditional ageing treatment, significantly enhancing both surface properties and bulk mechanical strength of the Ti-15-3 alloy.

3.4 Tribological performance evaluation

As described above, the designed novel IBTSF process successfully integrates bulk heat treatment with surface functionalisation via catalytic ceramic conversion treatment (C3T) to increase the bulk mechanical properties of the solution treated metastable β-titanium alloys by ~50%, while simultaneously forming a robust ceramic oxide layer that significantly enhances the surface hardness (**Figure 5**). To further evaluate the tribological performance of the treated samples, reciprocating wear tests were conducted on the 32 h samples, chosen for their thickest surface ceramic layers (**Figure 3**) and highest surface hardness values (**Figure 5a**), and the results are presented below.

ST-A32 – Although its bulk mechanical strength can be significantly enhanced by α precipitation strengthening (**Figure 4**), the absence of a protective surface layer caused direct contact between the Ti surface and the counterpart WC ball, resulting in severe material transfer (**Figure 7**) via adhesive wear. Therefore, ST-A32 exhibited the poorest tribological performance characterised by the widely fluctuating (0.3~0.8) coefficient of friction (COF) (**Figure 6a**), the largest

wear volume (**Figure 6b, c**), and the highest wear factor (**Figure 6d**) when tested under both 10 N and 20 N.

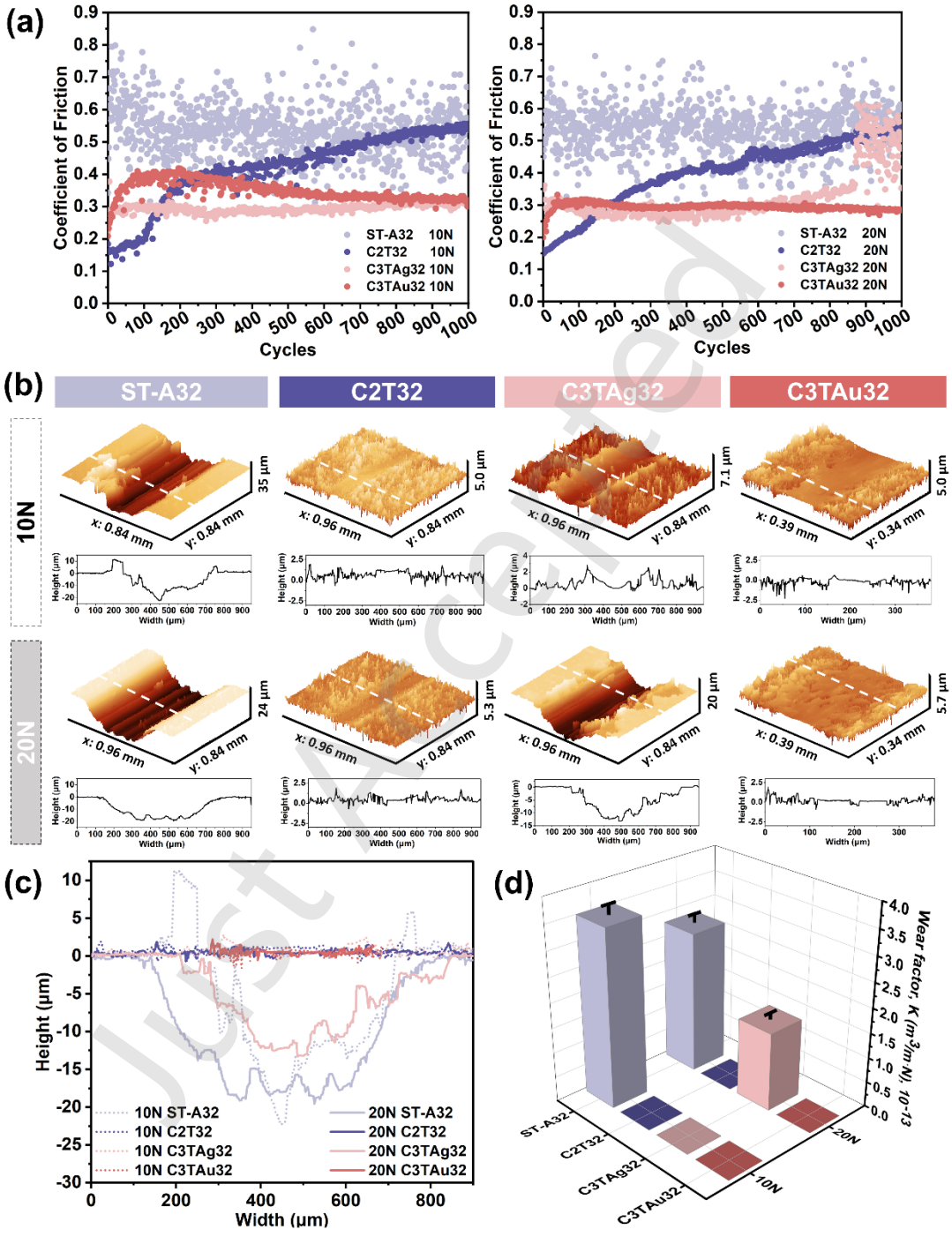

Figure 6. Wear tests results: (a) coefficient of frictions; (b) wear tracks topographies; (c) 2D wear tracks; (d) wear factors.

C2T32 – The hard ceramic oxide layer formed by C2T eliminated adhesive wear by preventing direct Ti-WC contact, which would otherwise occur due to the high chemical reactivity of Ti atoms [15, 33]. Instead, only abrasive wear could

be identified (**Figure 7**). The wear track was covered by a 0.8-1.0 μm thick tribo-film, making the wear volume and wear factor unmeasurable even under a high load of 20 N (**Figure 6d**). Although the COF distribution of C2T32 was much more stable than that of ST-A32, it increased steadily within 1000 cycles to exceed 0.5 (**Figure 6a**), indicating that C2T32 effectively transformed severe, unstable adhesive wear into milder abrasive wear but failed to reduce COF. This limitation is potentially due to the gradually exposure of the underlying ODZ, which is wear resistant but exhibits a high COF [45, 46].

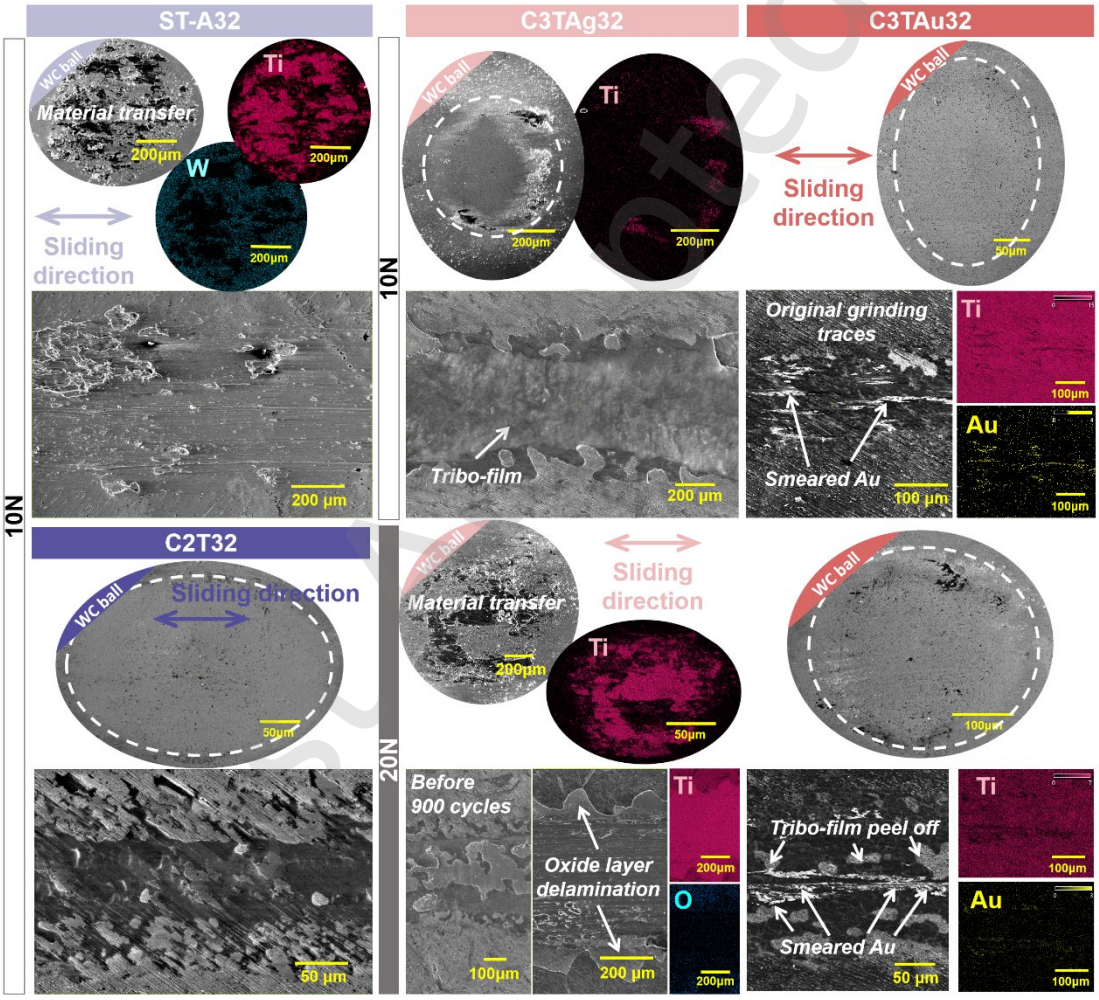

Figure 7. SEM and EDS analysis of the wear tracks and the counterpart balls for ST-A32, C2T32, C3TAg32 and C3TAu32.

C3TAg32 – The tribological performance of C3TAg32 depends on the applied loads. When tested for 1000 cycles under 10 N, a tribo-film was observed (**Figure 7**). The pile-up of the wear track edge without visible cracks (**Figure 6b**) suggests that the tribo-film has sufficient toughness due to the incorporation

of Ag and V in the surface layer (**Figure S3**), which not only reduced its brittleness but also enabled the film to provide dampening and potential lubricating effects [47] during sliding against the WC ball. Consequently, it exhibited tribological performance characterise by a stable and low COF around 0.3 (**Figure 6a)** and almost unmeasurable wear loss (**Figure 6b, c, d**). EDS of the counterpart WC ball revealed minor material transfer due to adhesive wear around the wear scar, while the absence of scratches along the sliding direction at the center of the wear scar indicated limited or no abrasive wear, further confirming the plasticity of the tribo-film formed on C3TAg32 under these conditions.

When the load increased to 20 N, the COF of C3TAg32 began to rise gradually after ~600 cycles, with tribo-film delamination being observed before 900 cycles (**Figure 7**). Between 900 and 1000 cycles, the COF became highly unstable, showing fluctuation similar to ST-A32 (**Figure 6a**). SEM and EDS (**Figure 7**) examination revealed features of severe adhesive wear on both the wear track and the WC ball, along with extensive oxide layer delamination near the wear track. The thickness of the delaminated oxide layer closely matched the total oxide thickness (~3 μm, **Section 3.3**), indicating almost complete removal of the oxide layer from the substrate, mainly arising due to the poor interfacial bonding. This weakness is possibly caused by the combination of the large oxide layer thickness (**Figure S4**) and high hardness (**Figure 5a**), which increased interfacial shear stress and promoted delamination. Thus, although no wear volume was measurable when tested under 10 N, the wear factor at 20 N reached 1.57×10^{-13} $m^3/(m\cdot N)$, exceeding that of C2T32 or C3TAu32.

C3TAu32 – As shown in **Figure 6**, C3TAu32 displayed near-zero wear under both 10 N and 20 N loads, accompanied by an extremely stable and low COF (~0.3). This outstanding tribological performance can be attributed to the plastic flow of Au particles on the oxide surface (**Figure S2**) under the combined compressive and shear action of the WC ball (**Figure 7**). These particles thereby acted as solid lubricants [33], maintaining the stable and low coefficient of friction and prolonging the life of the tribo-film formed during the tests.

3.5 *In Vitro* Antibacterial performance

To assess the antibacterial properties of the C2T and C3T samples, in vitro plate colony counting tests were performed. *S. aureus* and *E. coli* were selected as representative Gram-positive and Gram-negative strains, respectively.

As shown in **Figure 8a** (and in **Figure S5, S6, S7**), bacterial viability was significantly reduced on C3TAg surfaces compared with C3TAu and C2T surfaces. Quantitative analysis revealed that all C3TAg samples (C3TAg8, C3TAg16, and C3TAg32) achieved 99.999% antimicrobial efficacy against *S. aureus*, while C3TAg8 and C3TAg16 exhibited 95.854% and 98.537% reduction in colony forming *E. coli*, respectively. As no viable *E. coli* colonies were found on C3TAg32 samples after 6 h exposure, additional 3 h tests were performed and revealed 99.878% efficacy, even with the significantly reduced exposure time. This pronounced antibacterial performance is primarily attributed to the incorporation of Ag into the sample surface (**Figure 8b**), along with increased surface roughness (**Figure 2**), both of which contribute to sustained release of Ag^+ ions across an increased contact area. These ions disrupt bacterial metabolism by inactivating thiol-containing enzymes, binding to DNA, and increasing membrane permeability [48, 49]. Together, these mechanisms account for the broad-spectrum efficacy of the Ag-catalysed C3T surfaces.

Interestingly, the antimicrobial efficacy against *S. aureus* was consistently higher than that against *E. coli*, which is primarily due to structural differences between Gram-positive and Gram-negative bacteria. The thick but porous peptidoglycan layer of *S. aureus* facilitates Ag^+ penetration, whereas the outer lipopolysaccharide membrane of *E. coli* acts as an additional barrier, resulting in comparatively lower susceptibility [50]. The C2T samples exhibited ~60% inhibition of *S. aureus* but appeared to promote *E. coli* growth. This contrasting behaviour can be ascribed to differences in bacterial cell wall architecture and their interactions with the oxidised surface. The absence of an outer membrane in *S. aureus* renders it more vulnerable to surface-induced stress, leading to partial growth inhibition. In contrast, the outer lipopolysaccharide layer of *E. coli* not only provides protection but may also enhance bacterial adhesion to the oxidised surface, thereby facilitating proliferation [51].

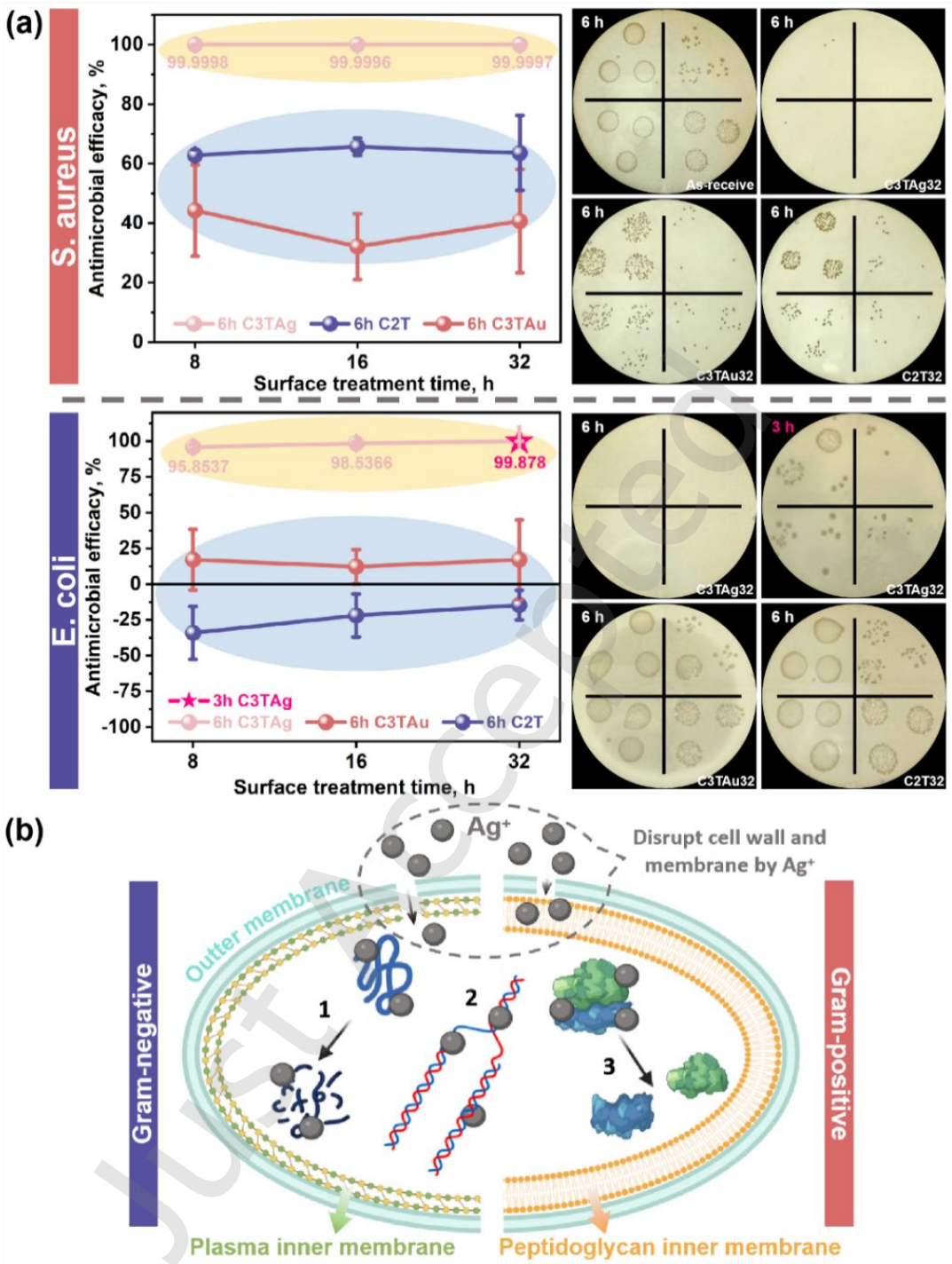

Figure 8. (a) Colony forming units of S. aureus and E. coli on C2T/C3T samples cultured for 6 h and a unit of E. coli on C3TAg32 cultured for 3 h; Calculated antibacterial efficacy rates of the samples; (b) Antibacterial mechanism: 1. Inhibition of translation of mRNA by binding to ribosomes; 2. Inhibition of replication machinery by binding to linear DNA; 3. Inhibition of protein enzymes [48, 49].

4. Discussion

This paper reports a novel surface engineering design that integrates bulk ageing heat treatment with surface functionalisation (IBTSF) through efficient Ag- or Au-facilitated catalytic ceramic conversion (C3T) technique, tailored for Ti-15-3 metastable β-titanium alloy. Unlike conventional surface engineering methods, in IBTSF both the bulk ageing treatment and the Ag/Au C3T surface multi-functionalisation occur simultaneously, effectively reducing processing steps, energy consumption, and manufacturing cost. Moreover, this IBTSF process not only confers surface functionality but also ensures the optimal bulk mechanical strength of β-titanium alloys, achieving a dual improvement in both surface and bulk properties. It is interesting to observe from the results reported in the preceding results section that both Au and Ag can promote ceramic conversion, increase surface hardness, improve tribological properties, and enhance antibacterial performance of Ti-15-3 metastable β-titanium alloy, although their effectiveness in promoting these multi-functions quantitatively differs.

Au promoted the formation of a dense oxide layer embedded with highly malleable Au particles, which acted as a solid lubricant and led to stable, low coefficients of friction under high loads. In contrast, Ag is more effective in catalysing the growth of thick mixed oxides with Ag-V surface features, which provided high antibacterial efficacy through Ag ion release, achieving a 99.878% antimicrobial efficacy within 3 h. These distinct outcomes indicate that the choice of catalyst governs not only oxidation kinetics but also the balance between tribological performance and antibacterial activity.

Therefore, the following section explores the potential mechanisms responsible for the distinct surface performance differences between Au-catalysed and Ag-catalysed IBTSF treated Ti-15-3 metastable β alloy.

4.1 Characteristics of surface oxide layers catalysed by Au and Ag

As reported in **Section 3**, the surface morphologies are distinctly different, being homogeneously smooth for C2T, decorated with Au particles for C3TAu, and covered with acicular Ag-V clusters for C3TAg samples (**Figure 2**). The cross-sectional layer structures (**Figure 3)** are similar, consisting of an oxide

layer atop an oxygen diffusion zone (ODZ), but the oxide layer produced by C3T (1.6-3.0 μm) is much thicker than that by C2T (0.8 μm). Among the C3T treatments, the oxide layer formed by C3TAg (~3.0 μm) is significantly thicker than that formed by C3TAu (1.6 μm), indicating a stronger catalytic effect by Ag as compared with Au.

To investigate the catalytic effect of Au and Ag on the characteristics of surface oxide layers, cross-sectional TEM specimens were prepared, and the STEM images with corresponding EDS mappings are presented in **Figure 9**.

It can be seen that both samples formed a distinct top layer followed by a similar nanocrystalline oxide layer. The top layer of the C3TAg32 sample consists of two sublayers from the surface inward, as distinguished by the STEM-EDS mappings: **(i)** a V, Ag, Cr and oxygen rich layer; **(ii)** a columnar layer enriched with Ti and oxygen (**Figure 9a**). Analysis of the SAD patterns identified Ag-V oxides in sublayer (i) and anatase-TiO_2 in sublayer (ii), clarifying the shape and distribution of the anatase detected in the XRD pattern (**Figure 4**). In contrast, the C3TAu32 sample showed a top layer of pure Au particles embedded within Ti (with V, Al and Cr) oxide grains approximately 250 nm in size (**Figure 9b**). Underneath the top layer, a nano-crystalline layer (10-50 nm) was formed. Indexing of the SAD patterns from this nano-crystalline layer identified rutile TiO_2 with traces of V, Cr, and Al oxides. TEM observation on C2T32 sample revealed a single oxide layer, similar to the nano-crystalline layer of the C3T samples (**Figure 9**), but with relatively larger grain sizes of 20-100nm (**Figure S8**).

It is clear that the pre-deposited thin Ag and Au films altered the surface oxide layer structure and thickness, introducing a distinct extra top sublayer, which likely contributed to accelerated surface layer growth. It is well-known that, driven by the strong affinity between Ti and oxygen, a thin titanium oxide film forms, especially when Ti is heated in air, and the subsequent oxidation process depends on the inward diffusion of O^{2-} and the outward diffusion of Ti^{4+} [47].

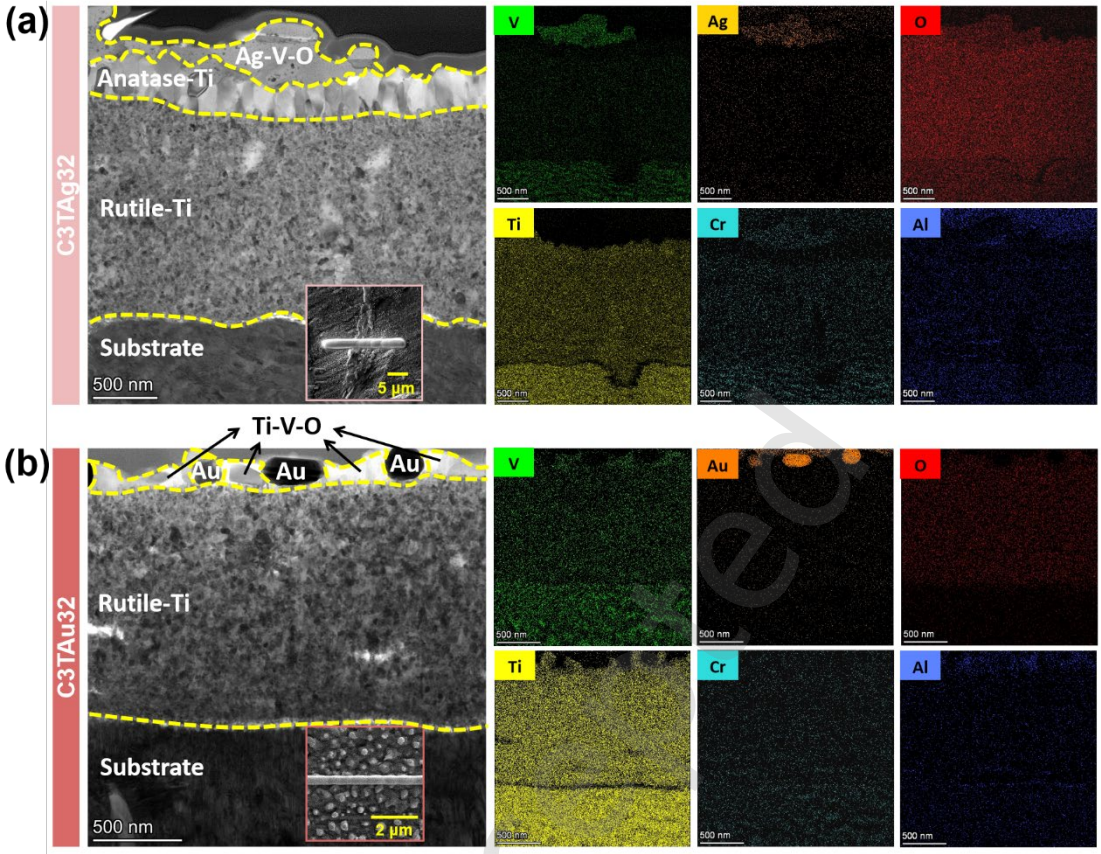

Figure 9. STEM images and corresponding EDS mappings of samples (a) C3TAg32, and (b) C3TAu32. Inserted in (a) and (b) are FIB cutting places with protected Pt layer.

The promotion of oxidation by surface Au likely due to two factors [33, 52, 53]: **1)** improving the oxygen adsorption efficiency on the titanium alloy surface by reducing the dissociation energy of adsorbed oxygen molecules, and **2)** accelerating the outward diffusion and activation of Ti^{4+}. This is supported by DFT calculations [33], which show that gold possesses higher electronegativity than titanium, thereby inducing significant electron extraction from the titanium atom and increasing the chemical activity of the titanium surface for the formation of titanium oxides.

According to the DFT calculations, the electron transfer of the Ti substrate (Δe) for Au and Ag is 4.42 e^- and 3.24 e^-, respectively, and hence the catalytic effect of Au would be expected to be stronger than that of Ag. However, as shown in **Figure 3**, the oxide layer formed by C3TAu is thinner than that formed by C3TAg. This seemingly contradictory observation is related to the strong interaction

between Ag and V, which forms acicular Ag-V oxide clusters observed on the C3TAg treated surfaces (**Figure 2**).

As shown in **Figure 9**, the pre-deposited Au layer was agglomerated into discrete Au particles, and Au and V remained separated on the C3TAu treated surface (**Figure 9b**), which significantly reduced the potential catalytic effect of Au during the C3TAu treatment. In contrast, as evidenced in the EDS mapping of **Figure 9a**, Ag and V co-existed to form Ag-V oxides, preventing agglomeration of Ag during the C3TAg treatment of Ti-15-3. Consequently, Ag could continuously facilitate electron extraction from the titanium atoms and enhance the chemical activity of the titanium surface for forming titanium oxides, thereby accelerating reaction and growth of surface oxide layers.

4.2 Wear mechanisms of C3TAu32 and C3TAg32

Based on the wear performance and the oxide layer microstructures presented in **Sections 3.3.4** and **4.1**, schematic diagrams of the wear mechanisms for C3TAu32 and C3TAg32 are constructed (**Figure 10**). The results shown in **Figure 5a** and **Figure 9** suggest that the exceptional hardness (~1200 HV) of C3TAg32 at low loads (≤100 g) could originate from its unique multilayered oxide structure with columnar grains. However, under a 20 N point-contact wear condition, the hard ceramic oxide layer with a high surface roughness (**Figure 2**, Ra) can fracture, producing hard fragmented wear debris that can act as abrasives (**Figure 7**). This can induce severe three-body abrasive wear between the treated surface and the WC ball faces, ultimately leading to surface failure (**Figure 10a**) and a high coefficient of friction after 900 cycles (**Figure 6a**).

In contrast, the surface oxide layer formed on C3TAu32 lacked obvious columnar features (**Figure 9b**); instead, Au nano-particles embedded within the surface (**Figure 2** and **Figure 9b**) acted as solid lubricants, while an Au-rich interfacial layer at the oxide/ODZ boundary buffered part of the applied contact stress. Consequently, C3TAu32 maintained a stable, low coefficient of friction and excellent wear resistance even under a high load of 20 N (**Figure 6a, d**).

Apart from the effect of microstructural differences in the oxide layer itself, the interfacial bonding strength between the oxide and the ODZ also played a

critical role. As shown in **Figure 7**, after 1000 cycles under 20 N, extensive delamination occurred near the wear track of C3TAg32, whereas no interfacial failure was observed for C3TAu32. The lower adhesion strength in C3TAg32 is likely due to the combination of its thick oxide layer (**Figure 3a**) and the modulus mismatch with the Ti substrate, which increased interfacial shear stress and promoted layer separation during friction.

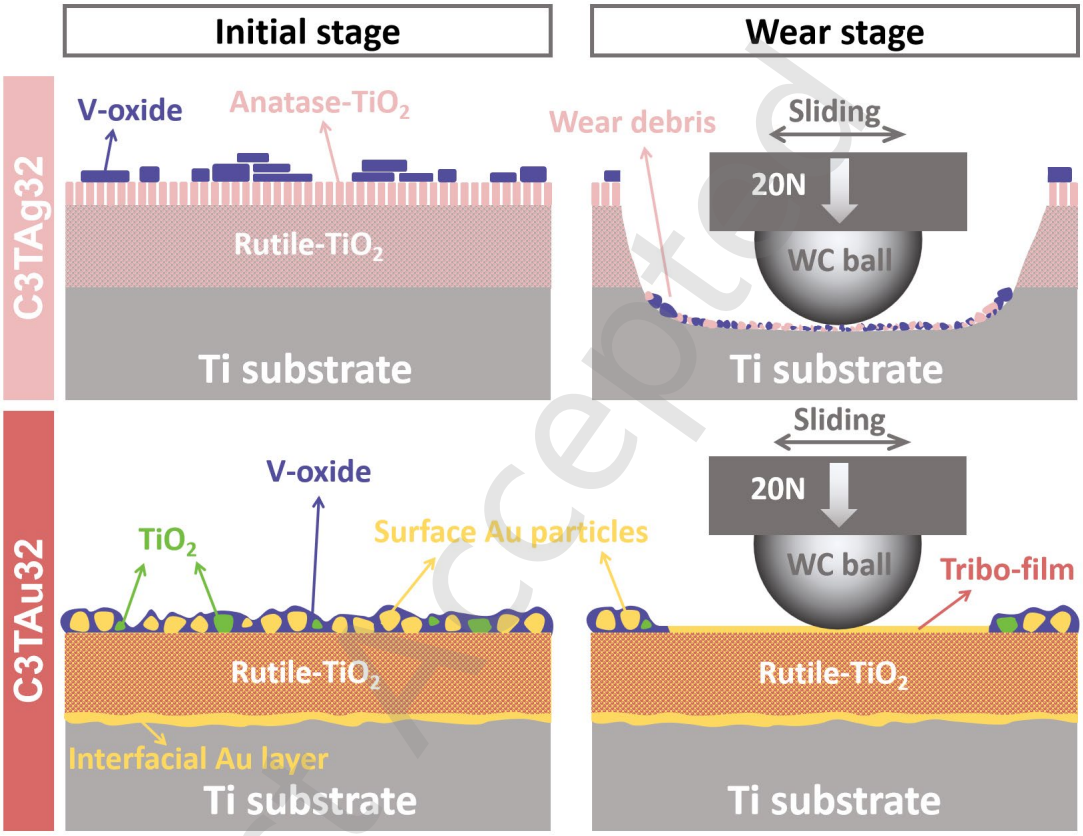

Figure 10. Different wear mechanisms: (a) C3TAg32 and (b) C3TAu32.

5. Summary and Conclusions

A novel surface engineering process has been designed by integrating bulk ageing treatment with surface functionalisation (IBTSF) through catalytic ceramic conversion with Ag (C3TAg) or Au (C3TAu) to generate multi-functional surfaces with high hardness, desirable tribological performance and high antibacterial efficacy in conjunction with superior bulk mechanical properties for Ti-15-3 metastable β alloy.

When treated under the same conditions, C3TAg produces a thicker and harder surface oxide layer with a columnar structure as compared with the oxide layer formed by C3TAu. When tested under 10N in wear experiments, both C3TAg and C3TAu treated samples exhibited similar superior tribological performance, with low COF (~0.3) and ultra-high wear resistance, comparable to solution and aged samples with the same thermal cycle. When wear tested under 20N, the C3TAu sample outperformed C3TAg.

The C3TAg treated samples achieved a high antibacterial efficacy of 99.878% and 99.999% within 3 h and 6 h tests against Gram-negative *E. coli* and Gram-positive *S. aureus* respectively.

Therefore, our study confirms the high potential of the IBTSF technology specifically designed for the surface functionalisation of metastable β-titanium alloys with simultaneous high bulk mechanical performance. By selectively tailoring catalytic conditions, β-titanium alloys can be engineered for either dual antibacterial–wear performance or ultra-high wear resistance, extending their application potential to biomedical implants, marine engineering systems, and sterile industrial machinery.

Acknowledgements

The authors would like to thank **XXX** for providing access to the Profilometry-Based Indentation Plastometry (PIP) facilities and **XXX** for the white-light interferometry measurements. XX acknowledges support from the National Natural Science Foundation of China (52501024) and from the Young Talent Support Project of Guangzhou Association for Science and Technology (No.QT-2025-041). The authors acknowledge the Centre for Electron Microscopy University of Birmingham for their support & assistance in this work. Figure 6b was created with BioRender.com.

References

[1] B. Zhang, J. Wang, B. Wu, X. Guo, Y. Wang, D. Chen, Y. Zhang, K. Du, E. Oguzie, X. Ma, Unmasking chloride attack on the passive film of metals, Nature communications 9(1) (2018) 2559.

[2] D. Yue, X. Jiang, H. Yu, D. Sun, In-situ fabricated hierarchical nanostructure on titanium alloy as highly stable and durable super-lubricated surface for anti-biofouling in marine engineering, Chemical Engineering Journal 463 (2023) 142389.

[3] J. Li, D. Zhang, X. Chen, D. Xu, D. Qiu, F. Wang, M. Easton, Laser directed energy deposited, ultrafine-grained functional titanium-copper alloys tailored for marine environments: Antibacterial and anti-microbial corrosion studies, Journal of Materials Science & Technology 166 (2023) 21-33.

[4] Z. Li, J. Wang, Y. Dong, D. Xu, X. Zhang, J. Wu, T. Gu, F. Wang, Synergistic effect of chloride ion and Shewanella algae accelerates the corrosion of Ti-6Al-4V alloy, Journal of Materials Science & Technology 71 (2021) 177-185.

[5] M. Sarraf, E. Rezvani Ghomi, S. Alipour, S. Ramakrishna, N. Liana Sukiman, A state-of-the-art review of the fabrication and characteristics of titanium and its alloys for biomedical applications, Bio-design and Manufacturing 5(2) (2022) 371-395.

[6] J. Toledano-Serrabona, B.M. Bosch, L. Díez-Tercero, F.J. Gil, O. Camps-Font, E. Valmaseda-Castellon, C. Gay-Escoda, M.Á. Sánchez-Garcés, Evaluation of the inflammatory and osteogenic response induced by titanium particles released during implantoplasty of dental implants, Scientific Reports 12(1) (2022) 15790.

[7] P. Jiang, Y. Zhang, R. Hu, B. Shi, L. Zhang, Q. Huang, Y. Yang, P. Tang, C. Lin, Advanced surface engineering of titanium materials for biomedical applications: From static modification to dynamic responsive regulation, Bioactive Materials 27 (2023) 15-57.

[8] S. Grosse, H.K. Haugland, P. Lilleng, P. Ellison, G. Hallan, P.J. Høl, Wear particles and ions from cemented and uncemented titanium-based hip prostheses—a histological and chemical analysis of retrieval material, Journal of Biomedical Materials Research Part B: Applied Biomaterials 103(3) (2015) 709-717.

[9] D.J. Hall, R. Pourzal, J.J. Jacobs, R.M. Urban, Metal wear particles in hematopoietic marrow of the axial skeleton in patients with prior revision for mechanical failure of a hip or knee arthroplasty, Journal of Biomedical Materials Research Part B: Applied Biomaterials 107(6) (2019) 1930-1936.
[10] G.E. Romanos, G.A. Fischer, R. Delgado-Ruiz, Titanium wear of dental implants from placement, under loading and maintenance protocols, international journal of molecular sciences 22(3) (2021) 1067.
[11] K. Apaza-Bedoya, M. Tarce, C.A. Benfatti, B. Henriques, M.T. Mathew, W. Teughels, J.C. Souza, Synergistic interactions between corrosion and wear at titanium-based dental implant connections: a scoping review, Journal of Periodontal Research 52(6) (2017) 946-954.
[12] H. Wu, X. Zhang, X. He, M. Li, X. Huang, R. Hang, B. Tang, Wear and corrosion resistance of anti-bacterial Ti–Cu–N coatings on titanium implants, Applied surface science 317 (2014) 614-621.
[13] M. Rahman, I. Reid, P. Duggan, D. Dowling, G. Hughes, M. Hashmi, Structural and tribological properties of the plasma nitrided Ti-alloy biomaterials: Influence of the treatment temperature, Surface and Coatings Technology 201(9-11) (2007) 4865-4872.
[14] M. Long, H. Rack, Titanium alloys in total joint replacement—a materials science perspective, Biomaterials 19(18) (1998) 1621-1639.
[15] D. Banerjee, J. Williams, Perspectives on titanium science and technology, Acta Materialia 61(3) (2013) 844-879.
[16] H. Dong, Tribological properties of titanium-based alloys, Surface engineering of light alloys, Elsevier2010, pp. 58-80.
[17] G. Zhao, J. Li, R. Zhang, H. Li, J. Li, L. Ma, Wear behavior of copper containing antibacterial stainless steel in different environmental media and EBSD analysis of its sub surface structure, Materials Characterization 197 (2023) 112690.
[18] Z. Ren, Y. Hu, Y. Tong, Z. Cai, J. Liu, H. Wang, J. Liao, S. Xu, L. Li, Wear-resistant NbMoTaWTi high entropy alloy coating prepared by laser cladding on TC4 titanium alloy, Tribology International 182 (2023) 108366.
[19] A.A. Siddiqui, A.K. Dubey, Recent trends in laser cladding and surface alloying, Optics & Laser Technology 134 (2021) 106619.

[20] H. Mohseni, P. Nandwana, A. Tsoi, R. Banerjee, T. Scharf, In situ nitrided titanium alloys: Microstructural evolution during solidification and wear, Acta Materialia 83 (2015) 61-74.
[21] W. Zhu, C. Zhao, Y. Zhang, C.T. Kwok, J. Luan, Z. Jiao, F. Ren, achieving exceptional wear resistance in a compositionally complex alloy via tuning the interfacial structure and chemistry, Acta Materialia 188 (2020) 697-710.
[22] D. Gu, Y.-C. Hagedorn, W. Meiners, G. Meng, R.J.S. Batista, K. Wissenbach, R. Poprawe, Densification behavior, microstructure evolution, and wear performance of selective laser melting processed commercially pure titanium, Acta materialia 60(9) (2012) 3849-3860.
[23] X. Ji, Y. Bao, S. Zhan, F. Wang, Y. Lai, Enhancing corrosive wear resistance and antibacterial properties of Ti6Al4V by laser-clad coatings with CrMoNbWCux powder, Intermetallics 185 (2025) 108927.
[24] J. Liu, H. Rong, R. Yang, Y. Zhang, Y. Hu, A. Dong, X. Wang, Y. Wang, D. Chen, K. Liu, A novel antibacterial and wear-resistant strategy based on metal surface micro-texture nitriding coupled functional mesoporous silicon coating, Surface and Coatings Technology 492 (2024) 131220.
[25] V. Kumar, R. Verma, S. Kango, V.S. Sharma, Recent progresses and applications in laser-based surface texturing systems, Materials Today Communications 26 (2021) 101736.
[26] H. Dong, T. Bell, Enhanced wear resistance of titanium surfaces by a new thermal oxidation treatment, Wear 238(2) (2000) 131-137.
[27] H. Dong, T. Bell, Tribological behaviour of alumina sliding against Ti6Al4V in unlubricated contact, Wear 225 (1999) 874-884.
[28] L.C. Zhang, L.Y. Chen, A review on biomedical titanium alloys: recent progress and prospect, Advanced engineering materials 21(4) (2019) 1801215.
[29] T. Zhang, Z. Huang, T. Yang, H. Kong, J. Luan, A. Wang, D. Wang, W. Kuo, Y. Wang, C.-T. Liu, In situ design of advanced titanium alloy with concentration modulations by additive manufacturing, Science 374(6566) (2021) 478-482.
[30] S. Guo, Q. Meng, X. Zhao, Q. Wei, H. Xu, Design and fabrication of a metastable β-type titanium alloy with ultralow elastic modulus and high strength, Scientific reports 5(1) (2015) 14688.
[31] X. Yang, C.R. Hutchinson, Corrosion-wear of β-Ti alloy TMZF (Ti-12Mo-6Zr-2Fe) in simulated body fluid, Acta biomaterialia 42 (2016) 429-439.

[32] T. Song, Z. Chen, X. Cui, S. Lu, H. Chen, H. Wang, T. Dong, B. Qin, K.C. Chan, M. Brandt, Strong and ductile titanium–oxygen–iron alloys by additive manufacturing, Nature 618(7963) (2023) 63-68.
[33] T. Pan, X. Li, Z. Zhang, Y. Yang, C. Liu, G. Qiao, H. Huang, H. Dong, A novel surface engineering technique for improving tribological performance of low-cost beta titanium alloy, Wear 572 (2025) 206076.
[34] E. Redmore, X. Li, H. Dong, Tribological performance of surface engineered low-cost beta titanium alloy, Wear 426 (2019) 952-960.
[35] J. Gupta, I.K. Jha, R.K. Khatirkar, J. Singh, Microstructure Evolution During Aging Heat Treatment of Metastable Ti-15V-3Cr-3Al-3Sn β Titanium Alloy, Journal of Materials Engineering and Performance (2025) 1-12.
[36] R. Gupta, V.A. Kumar, S. Chhangani, Study on variants of solution treatment and aging cycle of titanium alloy Ti6Al4V, Journal of Materials Engineering and Performance 25 (2016) 1492-1501.
[37] O. Ivasishin, P. Markovsky, Y.V. Matviychuk, S. Semiatin, Precipitation and recrystallization behavior of beta titanium alloys during continuous heat treatment, Metallurgical and Materials Transactions A 34(1) (2003) 147-158.
[38] C. Leyens, M. Peters, Titanium and titanium alloys: fundamentals and applications, Wiley Online Library2006.
[39] C. Knowles, T. Becker, R. Tait, Residual stress measurements and structural integrity implications for selective laser melted Ti-6Al-4V: General article, South African Journal of Industrial Engineering 23(3) (2012) 119-129.
[40] J. Ma, Q. Wang, Aging characterization and application of Ti–15–3 alloy, Materials Science and Engineering: A 243(1-2) (1998) 150-154.
[41] J. Campbell, R. Thompson, J. Dean, T. Clyne, Comparison between stress-strain plots obtained from indentation plastometry, based on residual indent profiles, and from uniaxial testing, Acta Materialia 168 (2019) 87-99.
[42] T. Southern, J. Campbell, C. Fang, A. Nemcova, A. Bannister, T. Clyne, Use of hardness, PIP and tensile testing to obtain stress-strain relationships for metals, Mechanics of Materials 187 (2023) 104846.
[43] E. Voce, The relationship between stress and strain for homogeneous deformation, Journal of the Institute of Metals 74 (1948) 537-562.

[44] X. Cen, X. Zhang, A.M. Thron, K. van Benthem, Agglomeration and long-range edge retraction for Au/Ni bilayer films during thermal annealing, Acta Materialia 119 (2016) 167-176.
[45] J. Qu, P.J. Blau, B.C. Jolly, Oxygen-diffused titanium as a candidate brake rotor material, Wear 267(5-8) (2009) 818-822.
[46] H. Dong, X. Li, Oxygen boost diffusion for the deep-case hardening of titanium alloys, Materials Science and Engineering: A 280(2) (2000) 303-310.
[47] S.M. Aouadi, D.P. Singh, D. Stone, K. Polychronopoulou, F. Nahif, C. Rebholz, C. Muratore, A.A. Voevodin, Adaptive VN/Ag nanocomposite coatings with lubricious behavior from 25 to 1000 C, Acta Materialia 58(16) (2010) 5326-5331.
[48] Z.-m. Xiu, Q.-b. Zhang, H.L. Puppala, V.L. Colvin, P.J. Alvarez, Negligible particle-specific antibacterial activity of silver nanoparticles, Nano letters 12(8) (2012) 4271-4275.
[49] S. Chernousova, M. Epple, Silver as antibacterial agent: ion, nanoparticle, and metal, Angewandte Chemie International Edition 52(6) (2013) 1636-1653.
[50] J.R. Morones-Ramirez, J.A. Winkler, C.S. Spina, J.J. Collins, Silver enhances antibiotic activity against gram-negative bacteria, Science translational medicine 5(190) (2013) 190ra81-190ra81.
[51] C.R. Arciola, D. Campoccia, P. Speziale, L. Montanaro, J.W. Costerton, Biofilm formation in Staphylococcus implant infections. A review of molecular mechanisms and implications for biofilm-resistant materials, Biomaterials 33(26) (2012) 5967-5982.
[52] Z. Zhang, Y. Zhang, X. Li, J. Alexander, H. Dong, An enhanced ceramic conversion treatment of Ti6Al4V alloy surface by a pre-deposited thin gold layer, Journal of Alloys and Compounds 844 (2020) 155867.
[53] T.A. Baker, X. Liu, C.M. Friend, The mystery of gold's chemical activity: local bonding, morphology and reactivity of atomic oxygen, Physical Chemistry Chemical Physics 13(1) (2011) 34-46.